# Toward a Genome Scale Dynamic Model of Cell-Free Protein Synthesis in *Escherichia coli*

Nicholas Horvath, Michael Vilkhovoy, Joseph Wayman, Kara Calhoun[1], James Swartz[1] and Jeffrey D. Varner[*]

Robert Frederick Smith School of Chemical and Biomolecular Engineering

Cornell University, Ithaca NY 14853

[1]School of Chemical Engineering

Stanford University, Stanford, CA 94305

**Running Title:** Dynamic modeling of cell-free protein synthesis

**To be submitted:** *Scientific Reports*

[*]Corresponding author:

Jeffrey D. Varner,

Professor, Robert Frederick Smith School of Chemical and Biomolecular Engineering,

244 Olin Hall, Cornell University, Ithaca NY, 14853

Email: jdv27@cornell.edu

Phone: (607) 255 - 4258

Fax: (607) 255 - 9166

## Abstract

Cell-free protein expression systems have become widely used in systems and synthetic biology. In this study, we developed an ensemble of dynamic *E. coli* cell-free protein synthesis (CFPS) models. Model parameters were estimated from measurements of glucose, organic acids, energy species, amino acids, and the protein product, chloramphenicol acetyltransferase (CAT). The ensemble described all of the training data, especially the central carbon metabolism. The model predicted CAT production with a carbon yield equal to 16%, and an energy efficiency equal to 9%, of that of a physiologically realistic case calculated using sequence-specific flux balance analysis. This suggests that CAT production could be further optimized. The dynamic modeling approach predicted that substrate consumption and oxidative phosphorylation were most important to both CAT production and the system as a whole, while CAT production alone depended heavily on the CAT synthesis reaction. Conversely, CAT production was robust to allosteric control, as was most of the network, with the exception of the organic acids in central carbon metabolism. This study is the first to model dynamic protein production in *E. coli*, and should provide a foundation for genome-scale, dynamic modeling of cell-free *E. coli* protein synthesis.

# Introduction

Cell-free systems offer many advantages for the study, manipulation and modeling of metabolism compared to *in vivo* processes. Central amongst these, is direct access to metabolites and the biosynthetic machinery without the interference of a cell wall, or complications associated with cell growth. This allows us to interrogate the chemical environment while the biosynthetic machinery is operating, potentially at a fine time resolution. Cell-free protein synthesis (CFPS) systems are arguably the most prominent examples of cell-free systems used today [1]. However, CFPS is not new; CFPS in crude *E. coli* extracts has been used since the 1960s to explore fundamentally important biological mechanisms [2, 3]. Today, cell-free systems are used in a variety of applications ranging from therapeutic protein production [4] to synthetic biology [5, 6]. However, if CFPS is to become a mainstream technology for applications such as point of care manufacturing, we must first understand the performance limits of these systems. One tool to address this question is mathematical modeling.

Mathematical modeling has long contributed to our understanding of metabolism. Decades before the genomics revolution, mechanistically structured metabolic models arose from the desire to predict microbial phenotypes resulting from changes in intracellular or extracellular states [7]. The single cell *E. coli* models of Shuler and coworkers pioneered the construction of large-scale, dynamic metabolic models that incorporated multiple, regulated catabolic and anabolic pathways constrained by experimentally determined kinetic parameters [8]. Shuler and coworkers generated many single cell kinetic models, including single cell models of eukaryotes [9, 10], minimal cell architectures [11], as well as DNA sequence based whole-cell models of *E. coli* [12]. In the post genomics world, large-scale stoichiometric reconstructions of microbial metabolism popularized by techniques such as flux balance analysis (FBA) have become a standard approach [13]. Since the first genome-scale stoichiometric model of *E. coli*, developed by Edwards and

Palsson [14], well over 100 organisms, including industrially important prokaryotes are now available [15–17]. Stoichiometric models rely on a pseudo-steady-state assumption to reduce unidentifiable genome-scale kinetic models to an underdetermined linear algebraic system, which can be solved efficiently even for large systems. Traditionally, stoichiometric models have also neglected explicit descriptions of metabolic regulation and control mechanisms, instead opting to describe the choice of pathways by prescribing an objective function on metabolism. Interestingly, similar to early cybernetic models, the most common metabolic objective function has been the optimization of biomass formation [18], although other metabolic objectives have also been estimated [19]. Recent advances in constraint-based modeling have overcome the early shortcomings of the platform, including capturing metabolic regulation and control [20]. Thus, modern constraint-based approaches have proven extremely useful in the discovery of metabolic engineering strategies and represent the state of the art in metabolic modeling [21, 22]. However, genome-scale kinetic models of industrial important organisms such as *E. coli* have yet to be constructed.

In this study, we developed an ensemble of kinetic cell-free protein synthesis (CFPS) models using dynamic metabolite measurements in an *E. coli* cell free extract. Model parameters were estimated from measurements of glucose, organic acids, energy species, amino acids, and the protein product, chloramphenicol acetyltransferase (CAT). Characteristic values for model parameters and initial conditions, estimated from literature, were used to constrain the parameter estimation problem. The ensemble of parameter sets described the training data with a median cost that was greater than two orders of magnitude smaller than random sets constructed using the literature parameter constraints. We then used the ensemble of kinetic models to analyze the CFPS reaction. First, sensitivity analysis of the dynamic model suggested that CAT production was most sensitive to CAT synthesis parameters, as well as reactions in oxidative phosphorylation and pyruvate

consumption. Sensitivity analysis also showed that the system as a whole was most sensitive to these same parts of the network and glucose consumption. CAT production and other metabolites, specifically organic acid intermediates such as pyruvate, were sensitive to the presence of allosteric control mechanisms. Next, to gauge the performance of the cell-free reaction, we compared the observed CAT carbon yield with the maximum theoretical CAT carbon yield calculated using sequence-specific flux balance analysis. The CAT yield estimated from the kinetic model was equal to 16% of the theoretical yield when physiologically realistic constraints were used. Taken together, we have integrated traditional kinetics with a logical rule-based description of allosteric control to simulate a comprehensive CFPS dataset. This study provides a foundation for genome-scale, dynamic modeling of cell-free *E. coli* protein synthesis.

## Results

The ensemble of kinetic CFPS models captured the time evolution of CAT biosynthesis (Fig. 1 - 3). The cell-free *E. coli* metabolic network was constructed by removing growth associated reactions from the *i*AF1260 reconstruction of K-12 MG1655 *E. coli* [16], and by adding reactions describing chloramphenicol acetyltransferase (CAT) biosynthesis, a model protein for which there exists a comprehensive training dataset [23]. In addition, reactions that were knocked out from the cell extract preparation were removed from the network (△speA, △tnaA, △sdaA, △sdaB, △gshA, △tonA, △endA). The CFPS model equations were formulated using the hybrid cell-free modeling framework of Wayman et al. [24]. An initial ensemble of model parameter sets (N > 5,000) was estimated from measurements of glucose, CAT, organic acids (pyruvate, lactate, acetate, succinate, malate), energy species (A(x)P, G(x)P, C(x)P, U(x)P), and 18 of the 20 proteinogenic amino acids using a constrained Markov Chain Monte Carlo (MCMC) approach. The MCMC algorithm minimized the error between the training data and model simulations starting from an initial parameter set assembled from literature and inspection. Parameter sets were selected for the final ensemble (N = 1,000) based upon their error and the Pearson correlation coefficient between the candidate and the existing sets in the ensemble; thus, an accurate yet diverse ensemble was created. The parameter set with the lowest error value was defined as the best-fit set. Central carbon metabolism (Fig. 1, top), energy species (Fig. 2), and amino acids (Fig. 3) were captured by the ensemble and the best-fit set. The constrained MCMC approach estimated parameter sets with a median error greater than two-order of magnitude less than random parameter sets generated within the same parameter bounds (Fig. 4); thus, we have confidence in the predictive capability of the estimated parameters. The model captured the biphasic CAT production: during the first hour glucose powers production, and CAT is produced at ~10 $\mu$M/h; subsequently, pyruvate and lactate reserves are consumed to power metabolism, and CAT

4

is produced less efficiently at ~5 $\mu$M/h. Allosteric control was important to central carbon metabolism, especially pyruvate and succinate, and to a lesser extent acetate and malate (Fig. 1, bottom). Taken together, we produced an ensemble of kinetic models that was consistent with time series measurements of the production of a model protein. Although the ensemble described the experimental data, it was unclear which kinetic parameters most influenced CAT production, and whether the performance of the CFPS reaction was optimal.

To better understand the effect of network reactions on system performance we conducted a group knockout analysis (Fig. 5). The network was divided into 19 groups of reactions, spanning central carbon metabolism, energetics, and amino aicd biosynthesis. The reactions in each of these groups were turned off, and the resulting change in cost function and system state were recorded. Then each pair of groups was knocked out to determine pairwise effects. These were summed with the first-order effect to obtain a total-order coefficient for each group for the change in cost function and system state.

The two largest total-order effects on the cost function are cysteine/methionine biosynthesis and anaplerotic/glyoxylate reactions. This is likely because... The effect of knocking out both of these reaction groups is understandably very great. However, the largest pairwise effect is seen when knocking out the Entner-Doudoroff pathway and the TCA cycle, two of the reaction groups with the smallest total-order effects. This is true of both the cost function knockout array and the system state knockout array. This may be because...

To better understand which parameters and parameter combinations influenced the performance of the kinetic model, we performed sensitivity analysis (Fig. 7). We perturbed each $V^{max}$ parameter, either individually or in pairwise combinations and measured the change in either CAT production or the overall system state. The eigen decomposition of the sensitivity shows that CAT synthesis and oxidative phosphorylation are the most important to overall CAT production, followed by the pyruvate-consuming alanine synthesis

5

reaction. Among the top 20 reactions, we saw a common theme of the cofactors ATP, NADH, NADPH, and coenzyme A, as well as the metabolites pyruvate, glutamate, and $\alpha$-ketoglutarate. ATP appears 7 times in these 20 reactions, while pyruvate, glutamate, and coenzyme A appear 6 times each. NADH, NADPH, and $\alpha$-ketoglutarate each appear 5 times. This result makes sense, as the high energy cost of protein synthesis means that energy cofactors played a crucial role. Also, pyruvate served as the primary substrate after glucose ran out, and pyruvate, glutamate, and $\alpha$-ketoglutarate were all important precursors for the synthesis of amino acids required by CAT production. We performed the same eigen decomposition on the sensitivity of the overall system state to network reactions (Fig. S1). Cytochrome oxidase, part of oxidative phosphorylation, was seen to have the greatest effect on the system state. Next most influential was the forward reaction of lactate dehydrogenase, followed by NADH:ubiquinone oxidoreductase, another oxidative phosphorylation reaction. The overall system state was also sensitive to cofactors and substrates, specifically NADH and pyruvate. Among the top 20 reactions, NADH appears in 8 reactions, pyruvate in 6, coenzyme A in 5, and ATP in 4. Glutamate, $\alpha$-ketoglutarate, G3P, and ubiquinone/ubiquinol appear 3 times each. Taken together, sensitivity analysis identified that substrates and energy cofactors, specifically those around oxidative phosphorylation, most influenced model performance.

To understand whether the CFPS performance was optimal, we calculated the carbon yield and energy efficiency of CAT production (Fig. 10). The best-fit parameter set for the kinetic model predicted a CAT carbon yield of 7.9%, while the experimental dataset had a CAT carbon yield of 8.2%. This was calculated as the increase in CAT concentration times the CAT carbon number, divided by the sum of the consumption terms for glucose and all amino acids excpet arginine and glutamate, as no data were available for these, weighted by their respective carbon numbers. To explain where the remainder of carbon was going, we performed a carbon balance for the best-fit set (Fig. 10A). Of the other 92% of carbon,

35% accumulated as organic acids (lactate, acetate, succinate and malate) and 9% accumulated as amino acids (alanine and glutamine). The remaining 48% went to the net accumulation of all other metabolites, particularly carbon dioxide. The best-fit set and the experimental dataset both produced CAT with an energy efficiency of 7% (Fig. 10B). This was calculated as the increase in CAT concentration times the CAT number of equivalent ATP molecules, divided by glucose consumption times times the number of equivalent ATP molecules for glucose, equal to 15 in the optimal case. An additional 62% of energy went to the accumulation of glycolysis metabolites, and 31% to organic acids (lactate, acetate, succinate and malate). This shows that there is much room for improvement of the efficiency of CFPS. Gene knockouts in the electron transport chain further reduced the performance of the CFPS reaction (Fig. 8). A key finding of both the CAT and overall system state sensitivity analysis was the importance of oxidative phosphorylation. To investigate this further, we knocked out key oxidative phosphorylation reactions in the ensemble of kinetic models to examine the effect on CAT production and carbon yield. A single *cyd* knockout reduced the CAT carbon yield from 7.9% to 2.6% (Table 1). On the other hand, a *nuo* knockout showed a less dramatic decrease in yield, reducing the CAT carbon yield to 6.9%. Knocking out *app* increased CAT yield to 8.1%, but this increase was not statistically significantly different from that of the control. Lastly, knocking out all three reactions reduced the CAT yield to 0.7%, similar to knocking out the *cyd* alone. Thus, the model suggested the key step in oxidative phosphorylation was catalyzed by the gene product of *cyd*. However, while disruption of *cyd* significantly reduced the CAT carbon yield, it did not completely eliminate the production of CAT. This suggested there was a mixture of energy sources supporting CAT production, with the most significant being oxidative phosphorylation.

Sequence-specific flux balance analysis (ssFBA) predicted optimal CAT yields with no adjustable parameters (Fig. 8). Before exploring CFPS optimality, we first validated the

7

ssFBA approach by comparing simulated and measured concentrations of CAT for the first hour of glucose consumption. We chose this time window (during the first phase of CAT production) because it was approximately linear both in glucose consumption and in the accumulation of most organic acids. As the ssFBA calculation had no adjustable parameters, bounds on transcription and translation rates and biochemical fluxes were either estimated from data or from mechanistic models parameterized from literature. Uncertainty in experimental factors such as RNA polymerase, ribosome concentrations, elongation rates, or the upper bounds for oxygen and glucose consumption rates was addressed by sampling plausible ranges for these parameters. The ensemble of ssFBA simulations predicted CAT formation as a function of time during the first hour of production when constrained by the experimental metabolite data (Fig. 8C). Thus, the molecular description of transcription and translation were consistent with experimental measurements. Next, to gauge the performance of the CFPS reaction, we next calculated the CAT carbon yield for three classes of constraints: (i) theoretical maximum glucose, amino acid and oxygen upper bounds, and realistic transcriptional/translational constraints; (ii) theoretical maximum glucose, amino acid and oxygen upper bounds, realistic transcriptional/translational constraints and knockouts of amino acid synthesis reactions of amino acids supplemented in the *E. coli* extract preparation. (iii) metabolite fluxes constrained by the CAT data, and realistic transcriptional/translational constraints and knockouts of amino acid synthesis reactions of amino acids supplemented in the *E. coli* extract preparation (Fig. 8D). The physiological theoretical maximum CAT carbon yield (case i) was 49.3% $\pm$ 3.5% (Fig. 8D, left); this represents optimal network performance if glucose, oxygen and amino acids were produced or consumed at their upper bounds, with bounded transcription and translation rates (96% without glucose contribution in the carbon yield calculation). For case ii, the optimal CAT carbon yield was 48.9% $\pm$ 3.5% (Fig. 8D, middle). Lastly, when metabolite constraints based on experimental measurements were applied (case iii), the predicted

8

carbon yield was 6.4% $\pm$ 2.9% (Fig. 8D, right). Unsurprisingly, this range of carbon yield encompasses both the best-fit set (7.9%) and the experimental dataset (8.2%). For cases i and ii the energy efficiencies were 72.1% $\pm$ 9.5% and 71.2% $\pm$ 9.6%, respectively, while for case iii it was only 5.1% $\pm$ 2.4%. This dramatic decrease in efficiency when fluxes are constrained to data makes sense, as the network is forced toward a multitude of pathways that may not contribute to CAT production. This range of energy efficiency encompasses both the best-fit set and the experimental dataset (7%). However, the model and the experimental dataset fall short of the optimum (cases i and ii). This suggests there is much room for improvement, primarily by reducing byproduct formation.

To investigate the differences in carbon yield and energy efficiency, we compared the flux distributions predicted by ssFBA simulations for the different constraint cases (Fig. 9). In cases i and ii, glycolysis was used for energy generation, and most of the carbon flux accumulated as acetate. The system produced NADH through lactate dehydrogenase as well as through pyridine nucleotide transhydrogenase (*pntAB*) to power oxidative phosphorylation. Case iii heavily utilized the first step in the pentose phosphate pathway to generate NADPH; the carbon flux then continued primarily through the Entner–Doudoroff pathway toward pyruvate. Case iii also predicted the accumulation of pyruvate, lacatate, acetate, and carbon dioxide, which contributed to the much lower carbon yield and energy efficiency. In all cases, the energy source was primarily oxidative phosphorylation converting cofactors generated throughout the network into ATP. Taken together, this suggested CAT production could be increased by reducing the accumulation of acetate, lactate, and carbon dioxide.

9

## Discussion

In this study we present an ensemble of *E. coli* cell-free protein synthesis (CFPS) models that accurately predict a comprehensive CFPS dataset of glucose, CAT, central carbon metabolites, energy species, and amino acid measurements. We used the hybrid cell-free modeling approach of Wayman and coworkers, which integrates traditional kinetic modeling with a logic-based description of allosteric regulation. CFPS is seen to be biphasic relying on glucose during the first hour and pyruvate and lactate afterward. Allosteric control was essential to the maintenance of the network and production of CAT, as without it, central carbon metabolism is exhuasted within 1.5 hours leading to low CAT production. Having captured the experimental data, we investigated if CAT yield and CFPS performance could be further improved. We showed that the model produces CAT with a carbon yield equal to 16% of that of a physiological case in which transcription and translation are constrained, and an energy efficiency equal to 9% of that of the physiological case. The accumulation of waste byproducts, especially acetate and carbon dioxide, is responsible for this sub-optimal performance. Sensitivity analysis showed that certain substrates and energy species are instrumental to CAT production and overall metabolism. The system heavily relied on oxidative phosphorylation for the system's energetic needs as well as for CAT synthesis. A single knockout in oxidative phosphorylation reduced the CAT carbon yield ~3-fold, as well as disrupting the system state, showing its crucial role in CFPS. In comparing flux distributions between low and high yield cases, carbon flux could be potentially diverted toward CAT by reducing acetate overflow and minimizing flux through the Entner-Doudoroff pathway. Taken together, these findings represent the first dynamic model of *E. coli* cell-free protein synthesis, and an important step toward a functional genome scale description.

We present an ensemble of models that quantitatively describes the system behavior of cell-free metabolism and production of CAT. Experimental observations of the metabo-

lites and cometabolites validate the structure of the model and the estimation of kinetic parameters. This is important in applying metabolic engineering principles to rationally design cell-free production processes and predict the redirection of carbon fluxes to product forming pathways. In analyzing the model parameters' effect on CAT production, CAT synthesis is the most important, followed by oxidative phosphorylation and the glutamate and pyruvate consuming reactions, as well as cofactor reactions which are necessary to drive CAT synthesis. For example, the conversion of ATP to GTP shows significance since it is necessary for CAT synthesis. While Jewett and coworkers have shown that ATP may be at saturation in CFPS [1], GTP is also required for CAT synthesis and may be a limiting reactant. Thus, supplementation with additional GTP may improve the efficiency of CAT production. A similar theme is seen in the sensitivity of overall model state, where the most important reactions are glucose and pyruvate consuming reactions and cofactor reactions which are vital to drive CFPS. This can be seen in the biphasic operation of CFPS, with the first phase operating on glucose and the second phase operating on pyruvate. During the first phase, there is an accumulation of byproducts from central carbon with the majority of flux going toward acetate and some toward pyruvate, lactate, and succinate; with the exception of acetate, these are all consumed in the second phase. This shows that CAT production can be sustained by pyruvate and glutamate in the absence of glucose, which provides alternative strategies to optimize CFPS performance. This is in accordance with literature, which showed pyruvate provided a relatively slow but continuous supply of ATP [25]. Taken together, this shows CFPS can be designed towards a specified application either requiring a slow stable energy source or faster production. This outstanding control on model performace was expected as these metabolites are responsible for driving CFPS and represent the first step in the model network. Nevertheless, there are further reactions with considerable impact on model performance. In examining oxidative phosphorylation activity, knockouts in the electron transport pathways disrupt metabolism

11

across the network and drop CAT carbon yield from 7.9% to 2.6%; Jewett and coworkers also saw a similar decrease in CAT yield with pyruvate as the substrate, ranging from 1.5-fold to 4-fold, when knocking out oxidative phosphorylation reactions [1]. Oxidative phosphorylation is vital, since it provides most of the energetic needs of CFPS. While it is unknown how active oxidative phosphorylation is compared to that of *in vivo* systems, both of our modeling approaches suggest its importance to improving CFPS performance and protein yield.

A logical next step for this work would be sequence-specific dynamic modeling, as the kinetic modeling approach in this study used a single reaction to approximate CAT synthesis. Including specific transcription and translation steps for CAT would allow more accurate modeling of the complexity and the resource cost of protein synthesis. Sensitivity analysis could then be performed on these new parameters to determine the robustness of CAT synthesis to the processes of transcription and translation. In addition, further experimentation could also be used to gain a deeper understanding of model performance under a variety of conditions. Specifically, CAT production performed in the absence of amino acids could inform the system's ability to manufacture them, while experimentation in the absence of glucose or oxygen could shed light on the importance of those substrates. Finally, the approach should be extended to other protein products. CAT is only a test protein used for model identification; the modeling framework, and to some extent the parameter values, should be protein agnostic. An important extension of this study would be to apply its insights to other protein applications, where possible.

### Materials and Methods

**Formulation and solution of the model equations.** We used ordinary differential equations (ODEs) to model the time evolution of metabolite ($x_i$) and scaled enzyme abundance ($\epsilon_i$) in hypothetical cell-free metabolic networks:

$$\frac{dx_i}{dt} = \sum_{j=1}^{\mathcal{R}} \sigma_{ij} r_j\left(\mathbf{x}, \epsilon, \mathbf{k}\right) \qquad i = 1, 2, \ldots, \mathcal{M} \tag{1}$$

$$\frac{d\epsilon_i}{dt} = -\lambda_i \epsilon_i \qquad i = 1, 2, \ldots, \mathcal{E} \tag{2}$$

where $\mathcal{R}$ denotes the number of reactions, $\mathcal{M}$ denotes the number of metabolites and $\mathcal{E}$ denotes the number of enzymes in the model. The quantity $r_j\left(\mathbf{x}, \epsilon, \mathbf{k}\right)$ denotes the rate of reaction $j$. Typically, reaction $j$ is a non-linear function of metabolite and enzyme abundance, as well as unknown kinetic parameters $\mathbf{k}$ ($\mathcal{K} \times 1$). The quantity $\sigma_{ij}$ denotes the stoichiometric coefficient for species $i$ in reaction $j$. If $\sigma_{ij} > 0$, metabolite $i$ is produced by reaction $j$. Conversely, if $\sigma_{ij} < 0$, metabolite $i$ is consumed by reaction $j$, while $\sigma_{ij} = 0$ indicates metabolite $i$ is not connected with reaction $j$. Lastly, $\lambda_i$ denotes the scaled enzyme activity decay constant. The system material balances were subject to the initial conditions $\mathbf{x}\left(t_o\right) = \mathbf{x}_o$ and $\epsilon\left(t_o\right) = \mathbf{1}$ (initially we have 100% cell-free enzyme abundance).

The reaction rate was written as the product of a kinetic term ($\bar{r}_j$) and a control term ($v_j$), $r_j\left(\mathbf{x}, \mathbf{k}\right) = \bar{r}_j v_j$. We used multiple saturation kinetics to model the reaction term $\bar{r}_j$:

$$\bar{r}_j = V_j^{max} \epsilon_i \prod_{s \in m_j^-} \frac{x_s}{K_{js} + x_s} \tag{3}$$

where $V_j^{max}$ denotes the maximum rate for reaction $j$, $\epsilon_i$ denotes the scaled enzyme activity which catalyzes reaction $j$, $K_{js}$ denotes the saturation constant for species $s$ in reaction $j$ and $m_j^-$ denotes the set of *reactants* for reaction $j$. On the other hand, the control term $0 \leq v_j \leq 1$ depended upon the combination of factors which influenced

rate process $j$. For each rate, we used a rule-based approach to select from competing control factors. If rate j was influenced by $1, \ldots, m$ factors, we modeled this relationship as $v_j = \mathcal{I}_j \left( f_{1j} \left( \cdot \right), \ldots, f_{mj} \left( \cdot \right) \right)$ where $0 \leq f_{ij} \left( \cdot \right) \leq 1$ denotes a transfer function quantifying the influence of factor $i$ on rate $j$. The function $\mathcal{I}_j \left( \cdot \right)$ is an integration rule which maps the output of regulatory transfer functions into a control variable. We used hill-like transfer functions and $\mathcal{I}_j \in \{min, max\}$ in this study [24].

We included 17 allosteric regulation terms, taken from literature, in the CFPS model. PEP was modeled as an inhibitor for phosphofructokinase [26, 27], PEP carboxykinase [26], PEP synthetase [26, 28], isocitrate dehydrogenase [26, 29], and isocitrate lyase/malate synthase [26, 29, 30], and as an activator for fructose-biphosphatase [26, 31–33]. AKG was modeled as an inhibitor for citrate synthase [26, 34, 35] and isocitrate lyase/malate synthase [26, 30]. 3PG was modeled as an inhibitor for isocitrate lyase/malate synthase [26, 30]. FDP was modeled as an activator for pyruvate kinase [26, 36] and PEP carboxylase [26, 37]. Pyruvate was modeled as an inhibitor for pyruvate dehydrogenase [26, 38, 39] and as an activator for lactate dehydrogenase [40]. Acetyl CoA was modeled as an inhibitor for malate dehydrogenase [26].

**Estimation of kinetic model parameters.**   We estimated an ensemble of diverse parameter sets using a constrained Markov Chain Monte Carlo (MCMC) random walk strategy. Starting from a single best fit parameter set estimated by inspection and literature, we calculated the cost function, equal to the sum-squared-error between experimental data and model predictions:

$$\texttt{cost} = \sum_{i=1}^{\mathcal{D}} \left[ \frac{w_i}{\mathcal{Y}_i^2} \sum_{j=1}^{\mathcal{T}_i} \left( y_{ij} - x_i|_{t(j)} \right)^2 \right] \tag{4}$$

where $\mathcal{D}$ denotes the number of datasets ($\mathcal{D}$ = 37), $w_i$ denotes the weight of the $i^{th}$ dataset, $\mathcal{T}_i$ denotes the number of timepoints in the $i^{th}$ dataset, $t(j)$ denotes the $j^{th}$ time-

point, $y_{ij}$ denotes the measurement value of the $i^{th}$ dataset at the $j^{th}$ timepoint, and $x_i|_{t(j)}$ denotes the simulated value of the metabolite corresponding to the $i^{th}$ dataset, interpolated to the $j^{th}$ timepoint. Lastly, the cost calculation was scaled by the maximum experimental value in the $i^{th}$ dataset, $\mathcal{Y}_i = \max_j (y_{ij})$. We then perturbed each model parameter between an upper and lower bound that varied by parameter type:

$$k_i^{new} = \min\left(\max\left(k_i \cdot \exp(a \cdot r_i), l_i\right), u_i\right) \qquad i = 1, 2, \ldots, \mathcal{P} \qquad (5)$$

where $\mathcal{P}$ denotes the number of parameters ($\mathcal{P}$ = 815), which includes 163 maximum reaction rates ($V^{max}$), 163 enzyme activity decay constants, 455 saturation constants ($K_{js}$), and 34 control parameters, $k_i^{new}$ denotes the new value of the $i^{th}$ parameter, $k_i$ denotes the current value of the $i^{th}$ parameter, $a$ denotes a distribution variance, $r_i$ denotes a random sample from the normal distribution, $l_i$ denotes the lower bound for that parameter type, and $u_i$ denotes the upper bound for that parameter type. Maximum reaction rates were bounded between 0 and 500,000 mM/h [41]. Assuming a total enzyme concentration of 5.0 $\mu$M, this corresponds to catalytic rate bounds of 0 and 27,780 s$^{-1}$. These bounds resulted in a median catalytic rate of 0.16 s$^{-1}$ across the ensemble. Enzyme activity decay constants were bounded between 0 and 1 h$^{-1}$, corresponding to half lives of 42 minutes and infinity; median = 25 h. Saturation constants were bounded between 0.001 and 10 mM; median = 0.16 mM. Control parameters (gains and orders) were left unbounded; gain median = 0.076, order median = 0.69. For each newly generated parameter set, we re-solved the balance equations and calculated the cost function. All sets with a lower cost (and some with higher cost) were accepted into the ensemble. After generating XXX sets, we selected N = 1000 sets with minimal set to set correlation to avoid over-sampling any region of parameter space.

**Sensitivity analysis of the kinetic CFPS model.** We determined the reactions most important to protein production by computing the local sensitivity of CAT concentration (denoted as CAT) to each individual maximum reaction rate, and each pair of maximum reaction rates in the network. The sensitivity index was formulated as:

$$\mathcal{S}_{ij}^{\texttt{CAT}} = \left\| \texttt{CAT}(p_i, p_j, t) - \texttt{CAT}(\alpha \cdot p_i, \alpha \cdot p_j, t) \right\|_2 \qquad i, j = 1, 2, \ldots \mathcal{P} \tag{6}$$

where $\mathcal{S}_{ij}^{\texttt{CAT}}$ denotes the sensitivity of CAT production to the $i^{th}$ and $j^{th}$ parameters, $\texttt{CAT}(p_i, p_j, t)$ denotes CAT concentration as a function of time and the $i^{th}$ and $j^{th}$ parameters, $\alpha$ denotes the perturbation factor, and $\mathcal{P}$ denotes the number of maximum reaction rates ($\mathcal{P}$ = 163). In calculating the pairwise sensitivities, each parameter was perturbed by 1%; first-order sensitivities ($i = j$) were subject to two 1% perturbations. Parameters and parameter combinations were stratified into five degrees of importance, from least to most sensitive.

Likewise, we determined which reactions were most important to global system performance by computing the sensitivity of all species for which data exists (denoted as X) to each maximum reaction rate in the network. In this case, each sensitivity index was formulated as:

$$\mathcal{S}_{ij}^{\texttt{X}} = \left\| \texttt{X}(p_i, p_j, t) - \texttt{X}(\alpha \cdot p_i, \alpha \cdot p_j, t) \right\|_2 \qquad i, j = 1, 2, \ldots \mathcal{P} \tag{7}$$
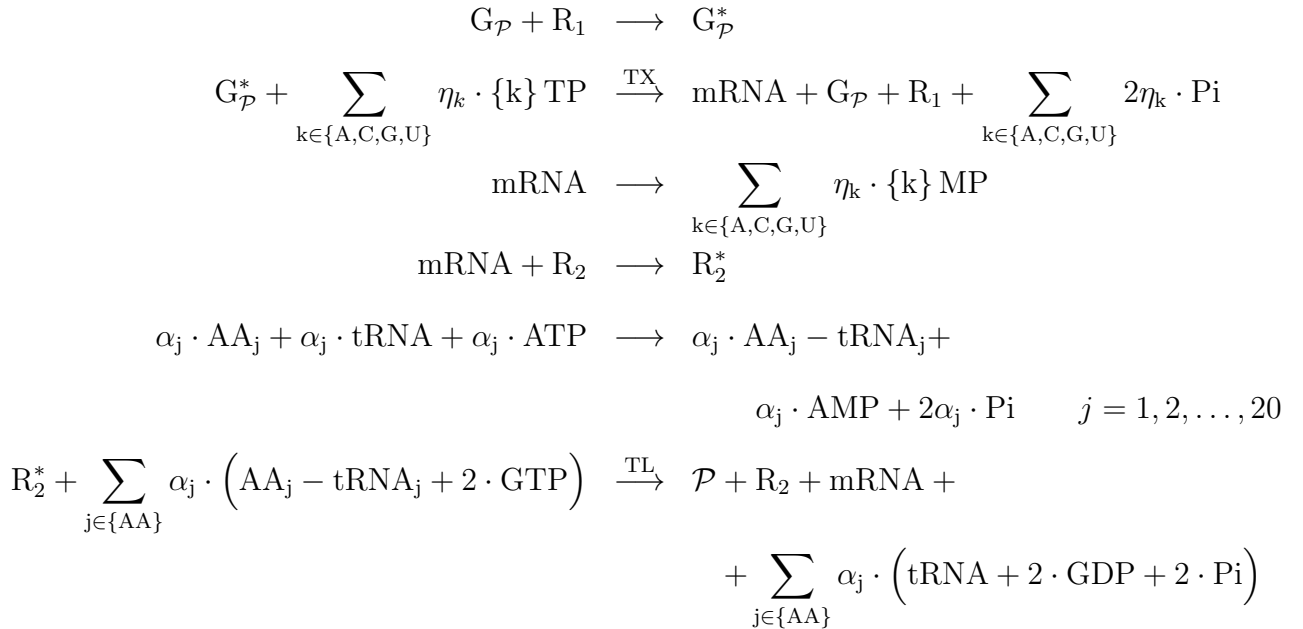
where $\mathcal{S}_{ij}^{\texttt{X}}$ denotes the sensitivity of the system state to the $i^{th}$ and $j^{th}$ parameters, and $\texttt{X}(p_i, p_j, t)$ denotes the system state, an array consisting of the concentration of every species for which data exists as a function of time and the $i^{th}$ and $j^{th}$ parameters. The parameter sensitivities were stratified into five degrees of importance, from least to most sensitive, as above.

16

**Sequence-specific calculation of carbon yield.** We estimated the theoretical maxi-

mum CAT carbon yield using sequence-specific flux balance analysis (ssFBA) [42]. The

sequence-specific flux balance analysis problem was formulated as a linear program:

$$\max_{\boldsymbol{w}} \left( w_{TL} = \boldsymbol{\theta}^T \boldsymbol{w} \right)$$
$$\text{Subject to}: \ \mathbf{Sw} = \mathbf{0} \tag{8}$$
$$\alpha_i \leq w_i \leq \beta_i \qquad i = 1, 2, \ldots, \mathcal{R}$$

where S denotes the stoichiometric matrix, $\mathbf{w}$ denotes the unknown flux vector, $\boldsymbol{\theta}$ denotes

the objective selection vector and $\alpha_i$ and $\beta_i$ denote the lower and upper bounds on flux $w_i$,

respectively. The stoichiometry of the kinetic model was used for the ssFBA calculations,

with the execpetion of the transcription and translation rates. The transcription (TX) and

translation (TL) stoichiometry was modeled using the template reactions taken from Allen

and Palsson [42]:

$$G_{\mathcal{P}} + R_1 \ \longrightarrow \ G_{\mathcal{P}}^*$$

$$G_{\mathcal{P}}^* + \sum_{k \in \{A,C,G,U\}} \eta_k \cdot \{k\} \, TP \ \xrightarrow{TX} \ mRNA + G_{\mathcal{P}} + R_1 + \sum_{k \in \{A,C,G,U\}} 2\eta_k \cdot Pi$$

$$mRNA \ \longrightarrow \ \sum_{k \in \{A,C,G,U\}} \eta_k \cdot \{k\} \, MP$$

$$mRNA + R_2 \ \longrightarrow \ R_2^*$$

$$\alpha_j \cdot AA_j + \alpha_j \cdot tRNA + \alpha_j \cdot ATP \ \longrightarrow \ \alpha_j \cdot AA_j - tRNA_j +$$

$$\alpha_j \cdot AMP + 2\alpha_j \cdot Pi \qquad j = 1, 2, \ldots, 20$$

$$R_2^* + \sum_{j \in \{AA\}} \alpha_j \cdot \left( AA_j - tRNA_j + 2 \cdot GTP \right) \ \xrightarrow{TL} \ \mathcal{P} + R_2 + mRNA +$$

$$+ \sum_{j \in \{AA\}} \alpha_j \cdot \left( tRNA + 2 \cdot GDP + 2 \cdot Pi \right)$$

where $G_{\mathcal{P}}$ denotes the gene encoding protein product $\mathcal{P}$, $\mathrm{R}_1$ denotes the concentration of RNA polymerase, $G_{\mathcal{P}}^*$ denotes the gene bounded by the RNA polymerase, $\eta_i$ and $\alpha_j$ denote the stoichiometric coefficients for nucleotide and amino acid, respectively, $\mathrm{Pi}$ denotes inorganic phosphate, $\mathrm{R}_2$ denotes the ribosome concentration, $\mathrm{R}_2^*$ denotes bounded ribosome, and $AA_j$ denotes $j^{th}$ amino acid.

The transcription rate ($w_{TX}$) was fixed in the ssFBA calculation at:

$$w_{TX} = V_{TX}^{max}\left(\frac{G}{K_{TX} + G}\right) \tag{9}$$

where $G$ denotes the gene concentration, and $K_{TX}$ denotes a transcription saturation coefficient. The maximum rate of transcription $V_{TX}^{max}$ was formulated as:

$$V_{TX}^{max} \equiv \left[R_1\left(\frac{v_{TX}}{l_G}\right)\left(\frac{K_{T7}}{1 + K_{T7}}\right)\right] \tag{10}$$

The term $R_1$ denotes the RNA polymerase abundance, $v_{TX}$ denotes the RNA polymerase elongation rate (nt/hr), $l_G$ denotes the gene length in nucleotides, and the last term describes T7 promoter activity, where $K_{T7}$ denotes a T7 RNA polymerase binding constant [43]. On the other hand, the translation rate ($w_{TL}$) was bounded by:

$$0 \leq w_{TL} \leq V_{TL}^{max}\left(\frac{\mathrm{mRNA_{SS}}}{K_{TL} + \mathrm{mRNA_{SS}}}\right) \tag{11}$$

where $\mathrm{mRNA_{SS}}$ denotes the steady state mRNA abundance, and $K_{TL}$ denotes the translation saturation constant. The maximum translation rate $V_{TL}^{max}$ was formulated as:

$$V_{TL}^{max} \equiv \left[K_P R_2\left(\frac{v_{TL}}{l_P}\right)\right] \tag{12}$$

The term $K_P$ denotes the polysome amplification constant, $v_{TL}$ denotes the ribosome

elongation rate (amino acids per hour), $l_P$ denotes the number of amino acids in the protein of interest, and $\mathrm{mRNA_{SS}}$ denotes the steady-state mRNA concentration:

$$\mathrm{mRNA_{SS}} \simeq \frac{\mathrm{w_{TX}}}{\lambda} \qquad (13)$$

where $\lambda$ denotes the rate constant controlling the mRNA degradation rate.

The objective of the sequence-specific flux balance calculation was to maximize the rate of CAT translation, $w_{TL}$. The total glucose uptake rate was bounded by [0,40 mM/h] according to experimental data; while the amino acid uptake rates were bounded by [0,30 mM/h], but did not reach the maximum flux. The CAT gene and protein sequences were taken from literature. The sequence-specific flux balance linear program was solved using the GNU Linear Programming Kit (GLPK) v4.52 [44].

*Quantification of uncertainty.* An ensemble of 1000 sets of flux distributions was calculated for three different cases: constrained by transcription/translation rates, constrained by transcription/translation rates without amino acid synthesis reactions, and constrained by transcription/translation rates and experimental measurements without amino acid synthesis reactions. For the first case, all rates were left unbounded, except the specific glucose uptake rate, transcription and translation rate. An ensemble of flux distributions was then calculated by randomly sampling the maximum specific glucose uptake rate from within a range of 30 to 40 mM/h, determined from experimental data and randomly sampling RNAP polymerase levels, ribosome levels, and elongation rates in a physiological range determined from literature.. For the second case, an ensemble was generated by randomly sampling the same parameters as the first case, however certain amino acid synthesis reactions were removed from the network. This included all the amino acids that were present in the preparation of the *E. coli* extract (alanine, arginine, aspartate, cysteine, glutamate, glutamine and serine were excluded from the media), thus reactions

420 producing the excluded amino acids were left in the network. RNA polymerase levels

420 were sampled between 60 and 80 nM, ribosome levels between 7 and 16 µM, the RNA

421 polymerase elongation rate between 20 and 30 nt/sec, and the ribosome elongation rate

422 between 1.5 and 3 aa/sec [45, 46]. For the third case, the ensemble was generated as

423 in the second case, in addition to the lower and upper bounds on the fluxes for the data-

424 informed metabolites were sampled within the range given by the experimental noise.

425 This included the data for glucose, organic acids, energy species, and amino acids; CAT

426 was not constrained by experimental data, but by the transcription/translation rates as

427 stated above.

**Calculation of the carbon yield.** The CAT carbon yield ($Y_C^{CAT}$) was calculated as the

429 ratio of carbon produced as CAT divided by the carbon consumed as reactants (glucose

430 and amino acids):

$$Y_C^{CAT} = \frac{\Delta \texttt{CAT} \cdot C_{CAT}}{\displaystyle\sum_{i=1}^{\mathcal{R}} \max(\Delta m_i, 0) \cdot C_{m_i}} \tag{14}$$

431 where $\Delta\texttt{CAT}$ denotes the abundance of CAT produced, $C_{CAT}$ denotes carbon number of

432 CAT, $\mathcal{R}$ denotes the number of reactants, $\Delta m_i$ denotes the amount of the $i^{th}$ reactant

433 consumed (never allowed to be negative), and $C_{m_i}$ denotes the carbon number of the

434 $i^{th}$ reactant. Arginine and glutamate were excluded from the yield calculations, as no

435 experimental measurements were available for these amino acids. Yield of the best-fit

436 parameter set and the experimental data were calculated by setting $\Delta\texttt{CAT}$ equal to the

437 final minus the initial CAT concentration, and setting $\Delta m_i$ equal to the initial minus the

438 final reactant concentration. The individual CAT production and substrate consumption

439 terms for the best-fit set, kinetic models with knockouts, and experimental data are shown

440 in Table 1. Total net consumption of amino acids and amino acid consumption via CAT

441 synthesis were calculated for the best-fit set (Table **??**). Total net consumption was cal-

20

culated as amino acid concentration at 0 hours minus concentration at 3 hours; it was negative if synthesis outweighed consumption. Consumption toward CAT was calculated as CAT concentration at 3 hours minus concentration at 0 hours, times the stoichiometric coefficient for that amino acid in the CAT synthesis reaction. The difference between these was defined as other consumption, equal to consumption from reactions other than CAT synthesis minus amino acid production.

**Calculation of energy efficiency.** Energy efficiency was calculated as the ratio of CAT production to glucose consumption, both in terms of equivalent ATP molecules:

$$\text{Efficiency} = \frac{\Delta \texttt{CAT} \cdot (2\left(\text{ATP}_{\text{TX}} + \text{CTP}_{\text{TX}} + \text{GTP}_{\text{TX}} + \text{UTP}_{\text{TX}}\right) + 2 \cdot \text{ATP}_{\text{TL}} + \text{GTP}_{\text{TL}})}{\Delta \texttt{GLC} \cdot \text{ATP}_{\text{GLC}}}$$

(15)

where $\text{ATP}_{\text{TX}}$, $\text{CTP}_{\text{TX}}$, $\text{GTP}_{\text{TX}}$, $\text{UTP}_{\text{TX}}$ denote the stoichiometric coefficients of each energy species for CAT transcription, $\text{ATP}_{\text{TL}}$, $\text{GTP}_{\text{TL}}$ denote the stoichiometric coefficients of ATP and GTP for CAT translation, $\Delta \texttt{GLC}$ denotes the glucose consumption, equal to the initial minus the final glucose concentration, and $\text{ATP}_{\text{GLC}}$ denotes the equivalent ATP number for glucose. $\text{ATP}_{\text{TX}}$ = 176, $\text{CTP}_{\text{TX}}$ = 144, $\text{GTP}_{\text{TX}}$ = 151, $\text{UTP}_{\text{TX}}$ = 189, $\text{ATP}_{\text{TL}}$ = 219, $\text{GTP}_{\text{TL}}$ = 438, $\text{ATP}_{\text{GLC}}$ = 15.

## Competing interests

The authors declare that they have no competing interests.

## Author's contributions

J.V directed the modeling study. K.C and J.S conducted the cell free protein synthesis experiments. J.V, J.W, and N.H developed the cell free protein synthesis mathematical model, and parameter ensemble. J.V and M.V performed the sequence-specific flux balance analysis calculations. The manuscript was prepared and edited for publication by J.S, N.H, M.V, J.W and J.V.

## Acknowledgements

## Funding

## References

1. Jewett MC, Calhoun KA, Voloshin A, Wuu JJ, Swartz JR. An integrated cell-free metabolic platform for protein production and synthetic biology. Mol Syst Biol. 2008;4:220. doi:10.1038/msb.2008.57.

2. Matthaei JH, Nirenberg MW. Characteristics and stabilization of DNAase-sensitive protein synthesis in E. coli extracts. Proc Natl Acad Sci U S A. 1961;47:1580–8.

3. Nirenberg MW, Matthaei JH. The dependence of cell-free protein synthesis in E. coli upon naturally occurring or synthetic polyribonucleotides. Proc Natl Acad Sci U S A. 1961;47:1588–602.

4. Lu Y, Welsh JP, Swartz JR. Production and stabilization of the trimeric influenza hemagglutinin stem domain for potentially broadly protective influenza vaccines. Proc Natl Acad Sci U S A. 2014;111(1):125–30. doi:10.1073/pnas.1308701110.

5. Hodgman CE, Jewett MC. Cell-free synthetic biology: thinking outside the cell. Metab Eng. 2012;14(3):261–9. doi:10.1016/j.ymben.2011.09.002.

6. Pardee K, Slomovic S, Nguyen PQ, Lee JW, Donghia N, Burrill D, et al. Portable, On-Demand Biomolecular Manufacturing. Cell. 2016;167(1):248–59.e12. doi:10.1016/j.cell.2016.09.013.

7. Fredrickson AG. Formulation of structured growth models. Biotechnol Bioeng. 1976;18(10):1481–6. doi:10.1002/bit.260181016.

8. Domach MM, Leung SK, Cahn RE, Cocks GG, Shuler ML. Computer model for glucose-limited growth of a single cell of Escherichia coli B/r-A. Biotechnol Bioeng. 1984;26(3):203–16. doi:10.1002/bit.260260303.

9. Steinmeyer DE, Shuler ML. Structured model for Saccharomyces cerevisiae. Chem Eng Sci. 1989;44:2017–30.

10. Wu P, Ray NG, Shuler ML. A single-cell model for CHO cells. Ann N Y Acad Sci. 1992;665:152–87.

23

11. Castellanos M, Wilson DB, Shuler ML. A modular minimal cell model: purine and pyrimidine transport and metabolism. Proc Natl Acad Sci U S A. 2004;101(17):6681–6. doi:10.1073/pnas.0400962101.

12. Atlas JC, Nikolaev EV, Browning ST, Shuler ML. Incorporating genome-wide DNA sequence information into a dynamic whole-cell model of Escherichia coli: application to DNA replication. IET Syst Biol. 2008;2(5):369–82. doi:10.1049/iet-syb:20070079.

13. Lewis NE, Nagarajan H, Palsson BØ. Constraining the metabolic genotype-phenotype relationship using a phylogeny of in silico methods. Nat Rev Microbiol. 2012;10(4):291–305. doi:10.1038/nrmicro2737.

14. Edwards JS, Palsson BØ. The Escherichia coli MG1655 in silico metabolic genotype: its definition, characteristics, and capabilities. Proc Natl Acad Sci U S A. 2000;97(10):5528–33.

15. Feist AM, Herrgård MJ, Thiele I, Reed JL, Palsson BØ. Reconstruction of biochemical networks in microorganisms. Nat Rev Microbiol. 2009;7(2):129–43. doi:10.1038/nrmicro1949.

16. Feist AM, Henry CS, Reed JL, Krummenacker M, Joyce AR, Karp PD, et al. A genome-scale metabolic reconstruction for Escherichia coli K-12 MG1655 that accounts for 1260 ORFs and thermodynamic information. Mol Syst Biol. 2007;3:121. doi:10.1038/msb4100155.

17. Oh YK, Palsson BØ, Park SM, Schilling CH, Mahadevan R. Genome-scale reconstruction of metabolic network in Bacillus subtilis based on high-throughput phenotyping and gene essentiality data. J Biol Chem. 2007;282(39):28791–9. doi:10.1074/jbc.M703759200.

18. Ibarra RU, Edwards JS, Palsson BØ. Escherichia coli K-12 undergoes adaptive evolution to achieve in silico predicted optimal growth. Nature. 2002;420(6912):186–9. doi:10.1038/nature01149.

19. Schuetz R, Kuepfer L, Sauer U. Systematic evaluation of objective functions for predicting intracellular fluxes in Escherichia coli. Mol Syst Biol. 2007;3:119. doi:10.1038/msb4100162.

20. Hyduke DR, Lewis NE, Palsson BØ. Analysis of omics data with genome-scale models of metabolism. Mol Biosyst. 2013;9(2):167–74. doi:10.1039/c2mb25453k.

21. McCloskey D, Palsson BØ, Feist AM. Basic and applied uses of genome-scale metabolic network reconstructions of Escherichia coli. Mol Syst Biol. 2013;9:661. doi:10.1038/msb.2013.18.

22. Zomorrodi AR, Suthers PF, Ranganathan S, Maranas CD. Mathematical optimization applications in metabolic networks. Metab Eng. 2012;14(6):672–86. doi:10.1016/j.ymben.2012.09.005.

23. Calhoun KA, Swartz JR. An Economical Method for Cell-Free Protein Synthesis using Glucose and Nucleoside Monophosphates. Biotechnology Progress. 2005;21(4):1146–53. doi:10.1021/bp050052y.

24. Wayman JA, Sagar A, Varner JD. Dynamic Modeling of Cell-Free Biochemical Networks Using Effective Kinetic Models. Processes. 2015;3(1):138. doi:10.3390/pr3010138.

25. Swartz J. A PURE approach to constructive biology. Nature Biotechnology. 2001;19:732–3.

26. Kotte O, Zaugg JB, Heinemann M. Bacterial adaptation through distributed sensing of metabolic fluxes. Mol Syst Biol. 2010;6:355.

27. Cabrera R, Baez M, Pereira HM, Caniuguir A, Garratt RC, Babul J. The crystal complex of phosphofructokinase-2 of Escherichia coli with fructose-6-phosphate: kinetic and structural analysis of the allosteric ATP inhibition. J Biol Chem. 2011;286(7):5774–83.

28. Chulavatnatol M, Atkinson DE. Phosphoenolpyruvate synthetase from Escherichia

25

coli. Effects of adenylate energy charge and modifier concentrations. J Biol Chem. 1973;248(8):2712–5.

29. Ogawa T, Murakami K, Mori H, Ishii N, Tomita M, Yoshin M. Role of phospho-enolpyruvate in the NADP-isocitrate dehydrogenase and isocitrate lyase reaction in Escherichia coli. J Bacteriol. 2007;189(3):1176–8.

30. MacKintosh C, Nimmo HG. Purification and regulatory properties of isocitrate lyase from Escherichia coli ML308. Biochem J. 1988;250(1):25–31.

31. Donahue JL, Bownas JL, Niehaus WG, Larson TJ. Purification and characteriza-tion of glpX-encoded fructose 1, 6-bisphosphatase, a new enzyme of the glycerol 3-phosphate regulon of Escherichia coli. J Bacteriol. 2000;182(19):5624–7.

32. Hines JK, Fromm HJ, Honzatko RB. Novel allosteric activation site in Escherichia coli fructose-1,6-bisphosphatase. J Biol Chem. 2006;281(27):18386–93.

33. Hines JK, Fromm HJ, Honzatko RB. Structures of activated fructose-1,6-bisphosphatase from Escherichia coli. Coordinate regulation of bacterial metabolism and the conservation of the R-state. J Biol Chem. 2007;282(16):11696–704.

34. Pereira DS, Donald LJ, Hosfield DJ, Duckworth HW. Active site mutants of Es-cherichia coli citrate synthase. Effects of mutations on catalytic and allosteric proper-ties. J Biol Chem. 1994;269(1):412–7.

35. Robinson MS, Easom RA, Danson MJ, Weitzman PD. Citrate synthase of Escherichia coli. Characterisation of the enzyme from a plasmid-cloned gene and amplification of the intracellular levels. FEBS Lett. 1983;154(1):51–4.

36. Zhu T, Bailey MF, Angley LM, Cooper TF, Dobson RC. The quaternary structure of pyruvate kinase type 1 from Escherichia coli at low nanomolar concentrations. Biochimie. 2010;92(1):116–20.

37. Wohl RC, Markus G. Phosphoenolpyruvate carboxylase of Escherichia coli. Purifica-tion and some properties. J Biol Chem. 1972;247(18):5785–92.

38. Kale S, Arjunan P, Furey W, Jordan F. A dynamic loop at the active center of the Escherichia coli pyruvate dehydrogenase complex E1 component modulates substrate utilization and chemical communication with the E2 component. J Biol Chem. 2007;282(38):28106–16.

39. Arjunan P, Nemeria N, Brunskill A, Chandrasekhar K, Sax M, Yan Y, et al. Structure of the pyruvate dehydrogenase multienzyme complex E1 component from Escherichia coli at 1.85 A resolution. Biochemistry. 2002;41(16):5213–21.

40. Okino S, Suda M, Fujikura K, Inui M, Yukawa H. Production of D-lactic acid by Corynebacterium glutamicum under oxygen deprivation. Appl Microbiol Biotechnol. 2008;78(3):449–54.

41. Milo R, Jorgensen P, Moran U, Weber G, Springer M. BioNumbers–the database of key numbers in molecular and cell biology. Nucleic Acids Res. 2009;38:750–3.

42. Allen TE, Palsson BØ. Sequence-based analysis of metabolic demands for protein synthesis in prokaryotes. J Theor Biol. 2003;220(1):1–18.

43. Moon TS TASBVC Lou C. Genetic programs constructed from layered logic gates in single cells. Nature. 2012;491.

44. type; 2016. Available from: http://www.gnu.org/software/glpk/glpk.html.

45. Underwood KA, Swartz JR, Puglisi JD. Quantitative polysome analysis identifies limitations in bacterial cell-free protein synthesis. Biotechnology and Bioengineering. 2005;91(4):425–35. doi:10.1002/bit.20529.

46. Garamella J, Marshall R, Rustad M, Noireaux V. The All E. coli TX-TL Toolbox 2.0: A Platform for Cell-Free Synthetic Biology. ACS Synth Biol. 2016;5(4):344–55. doi:10.1021/acssynbio.5b00296.
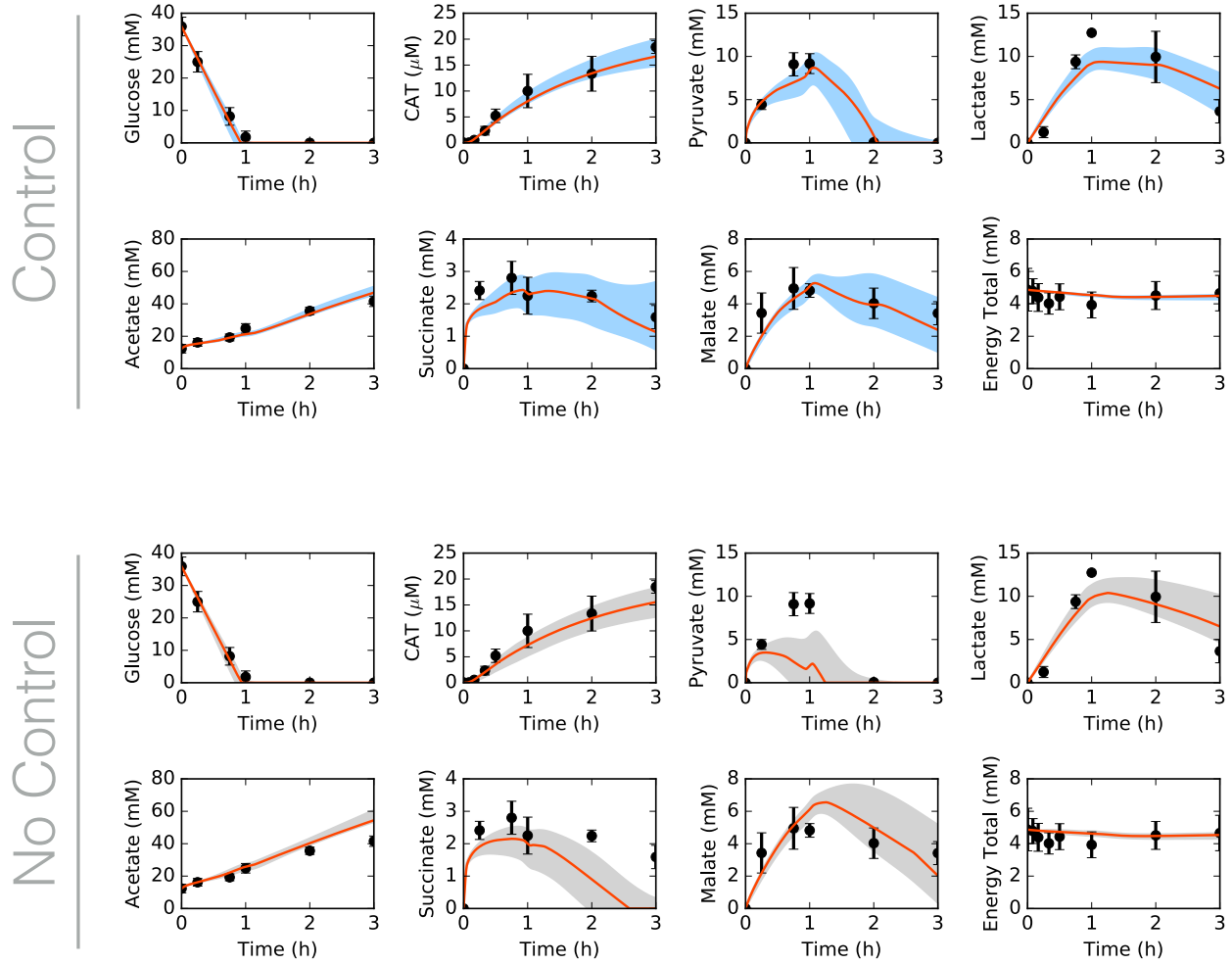
**Fig. 1:** Central carbon metabolism in the presence (top) and absence (bottom) of allosteric control, including glucose (substrate), CAT (product), and intermediates, as well as total concentration of energy species. Best-fit parameter set (orange line) versus experimental data (points). 95% confidence interval (blue or gray shaded region) over the ensemble of 1000 sets.
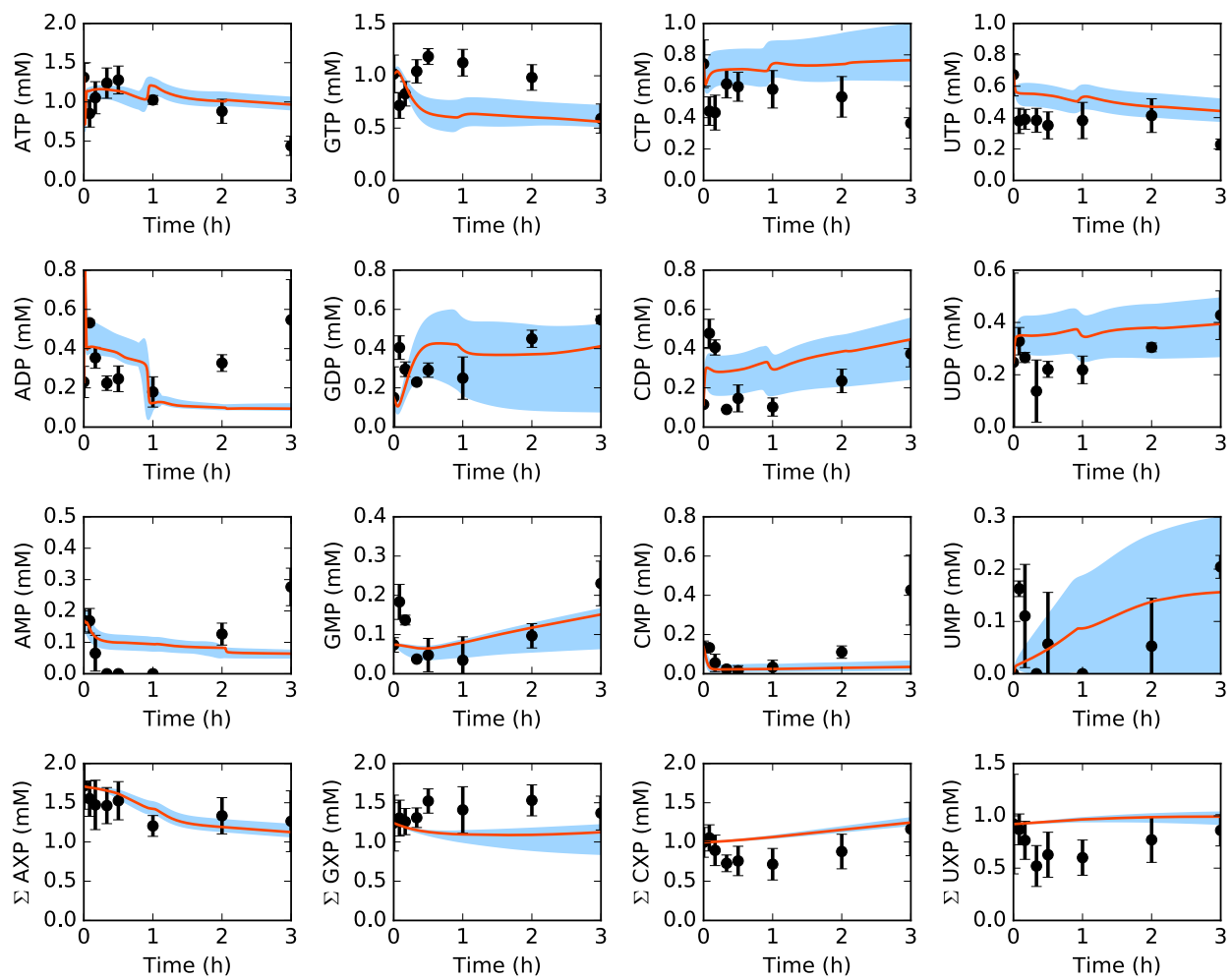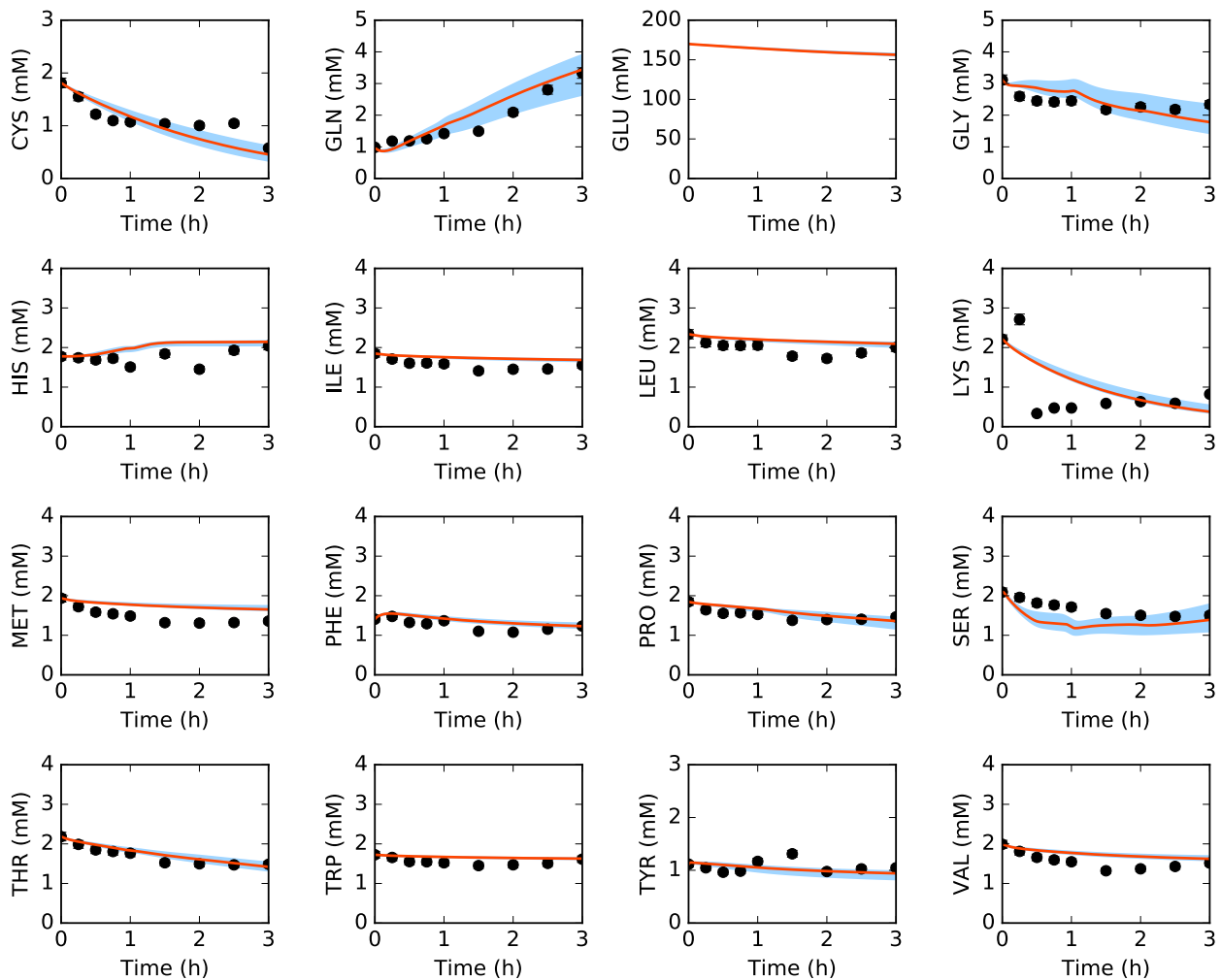
**Fig. 2:** Energy species and energy totals by base in the presence of allosteric control. Best-fit parameter set (orange line) versus experimental data (points). 95% confidence interval (blue shaded region) over the ensemble of 1000 sets.

**Fig. 3:** Amino acids in the presence of allosteric control. Best-fit parameter set (orange line) versus experimental data (points). 95% confidence interval (blue shaded region) over the ensemble of 1000 sets.
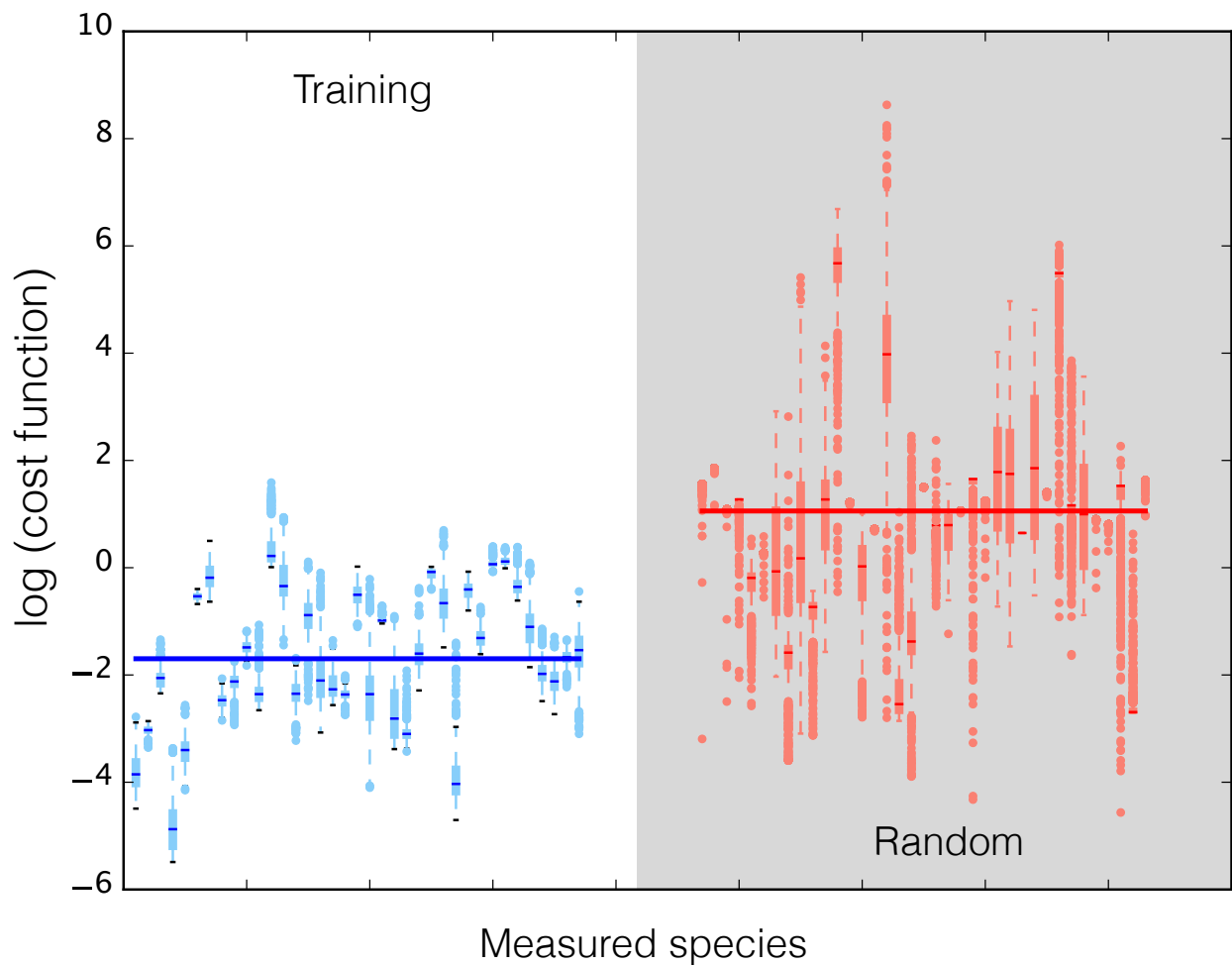
**Fig. 4:** Log of cost function across 37 datasets for data-trained ensemble (blue) and randomly generated ensemble (red, gray background). Median (bars), interquartile range (boxes), range excluding outliers (dashed lines), and outliers (circles) for each dataset. Median across all datasets (large bar overlaid).
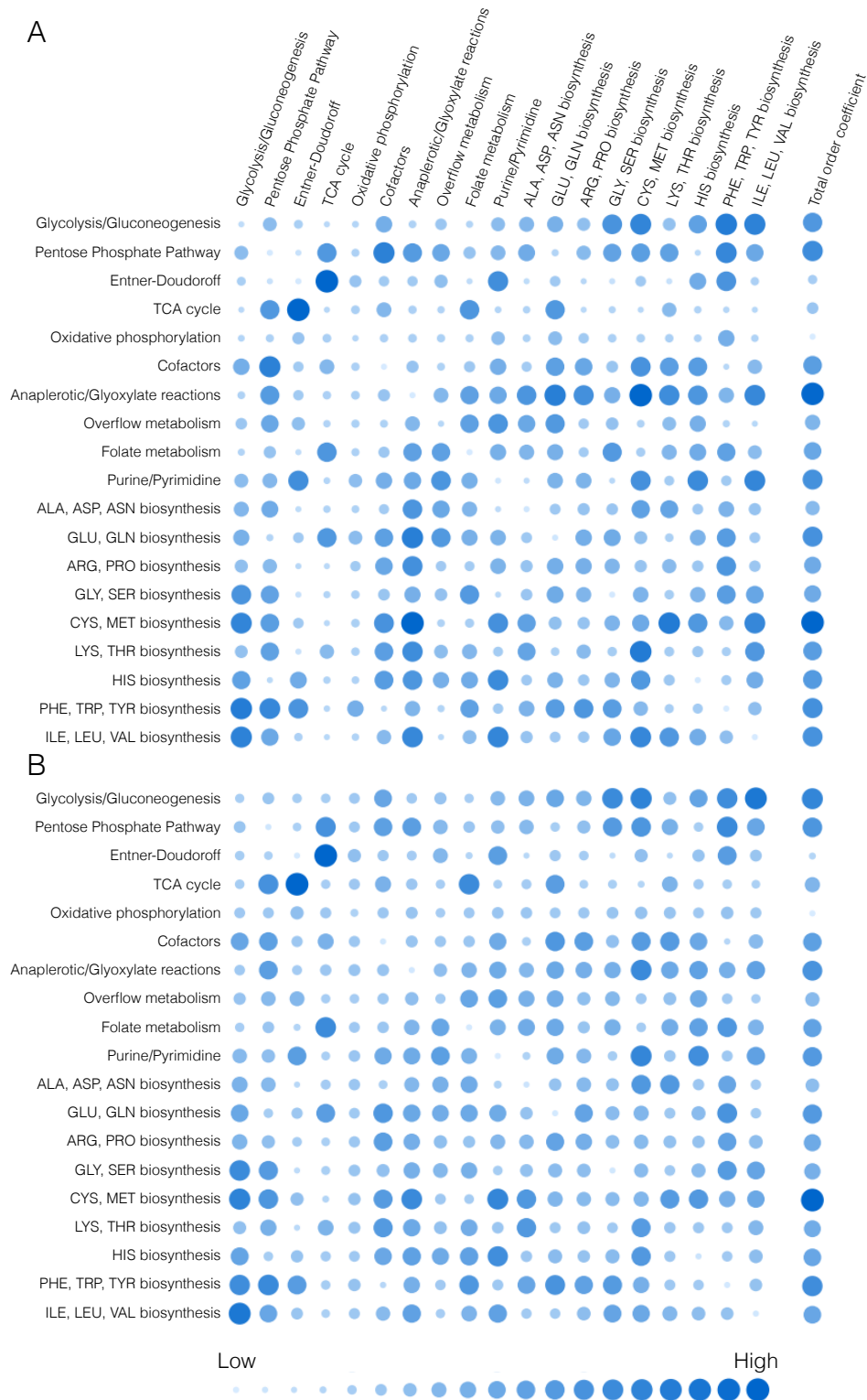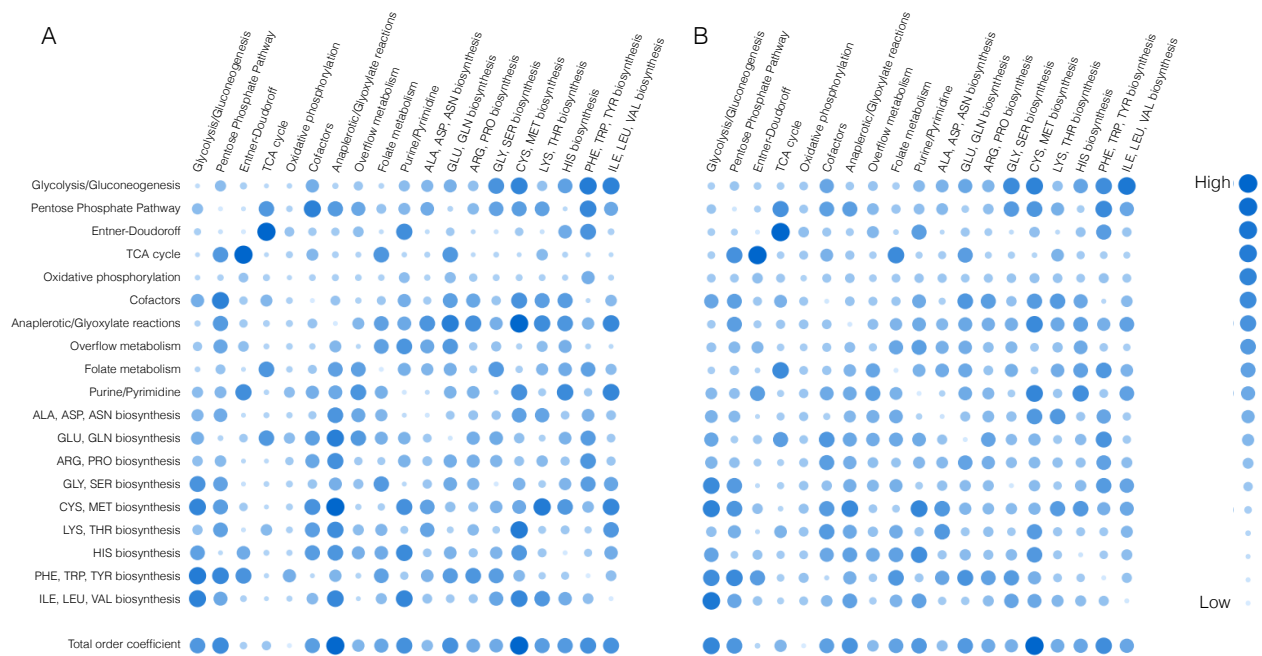
**Fig. 5:** Effect of group knockouts on system. A. Log change in cost function when one (diagonal) or two (off-diagonal) reaction groups are turned off. B. Log change in system state (only species for which data exist) when one (diagonal) or two (off-diagonal) reaction groups are turned off. Total-order effect for each group calculated as the sum of first-order effect and all pairwise effects. Larger and darker circles represent a greater effect.

**Fig. 6:** Effect of group knockouts on system. A. Log change in cost function when one (diagonal) or two (off-diagonal) reaction groups are turned off. B. Log change in system state (only species for which data exist) when one (diagonal) or two (off-diagonal) reaction groups are turned off. Total-order effect for each group calculated as the sum of first-order effect and all pairwise effects. Larger and darker circles represent a greater effect.
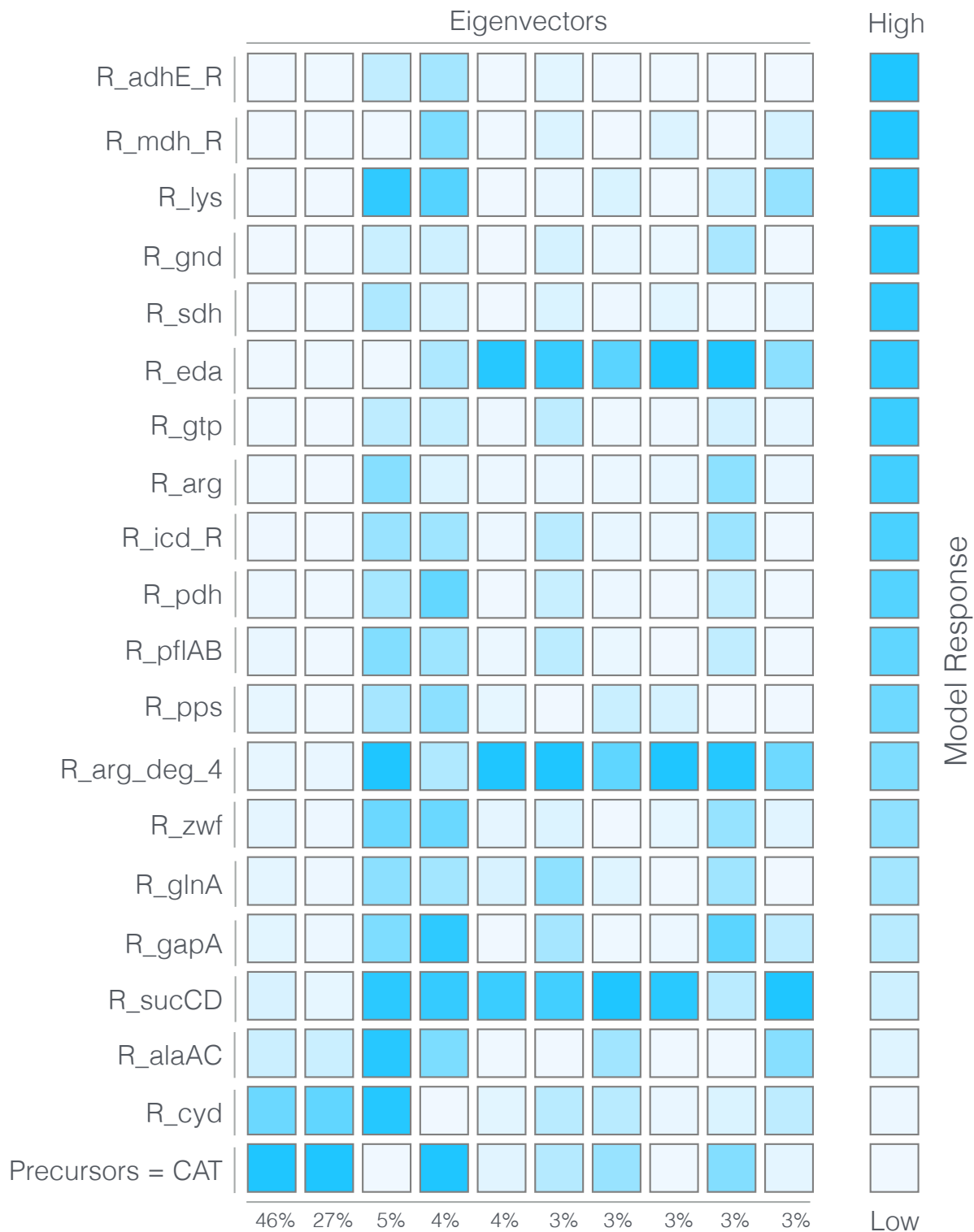
**Fig. 7:** Sensitivity of CAT production to model parameters, decomposed into eigenmodes. Sensitivity of top 10 eigenvectors (columns, left to right) to top 20 most influential parameters (rows, bottom to top). Relative magnitudes of eigenvalues expressed as percentages.
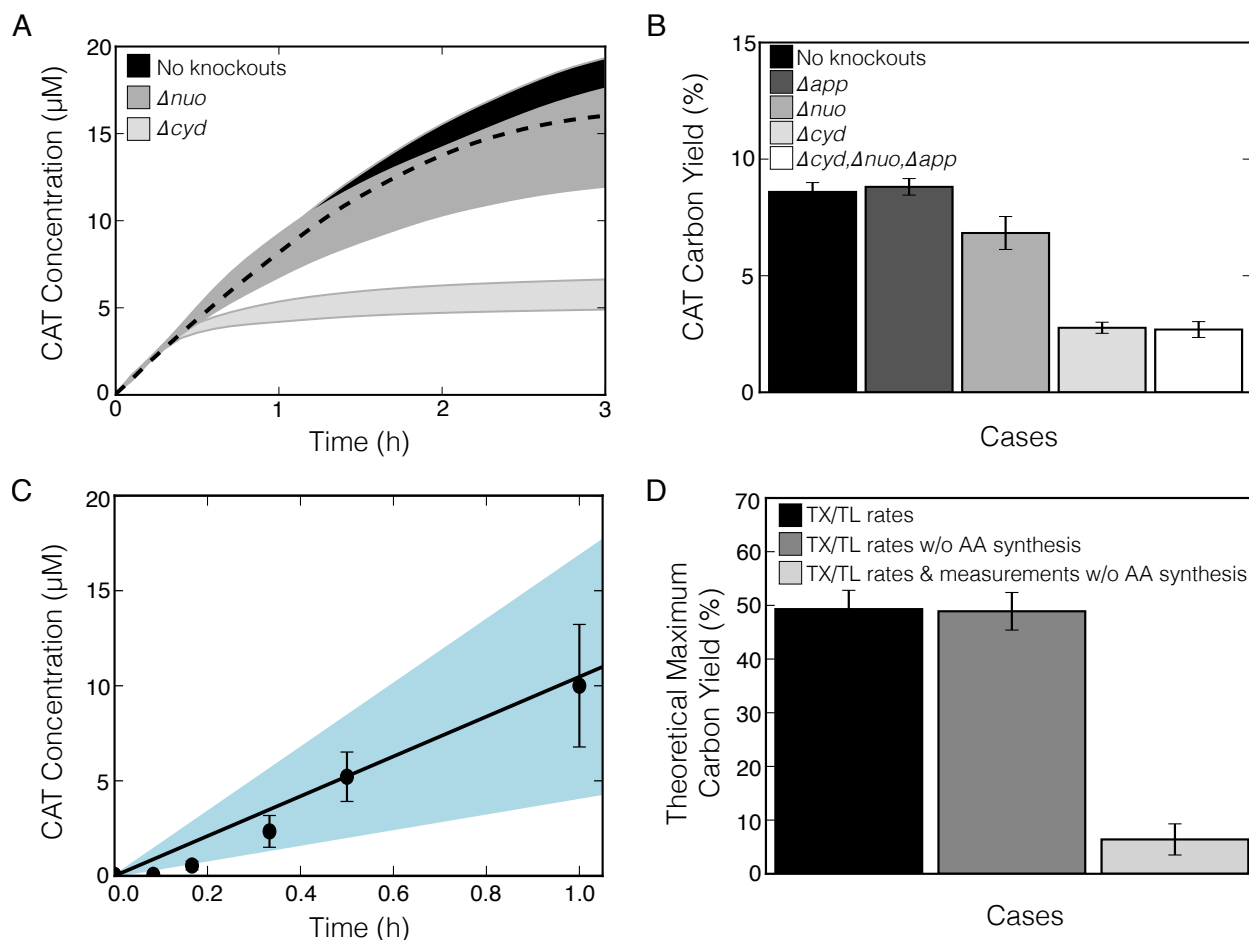
**Fig. 8:** The effects of oxidative phosphorylation and amino acid synthesis pathways on CAT production and carbon yield. A. 95% confidence interval of the ensemble of kinetic models for CAT concentration versus time, for the best-fit set with no knockouts (black shaded region and dashed line), *nuo* knockout (medium gray), and *cyd* knockout (light gray). B. CAT carbon yield of the ensemble of kinetic models for no knockouts (black), *app* knockout (dark gray), *nuo* knockout (medium gray), *cyd* knockout (light gray), and all three knockouts (white). Error bars represent standard deviation of the ensemble. C. 95% confidence interval of the ensemble of ssFBA simulations (light blue region) of CAT concentration over time, against experimental data (black). D. Theoretical maximum carbon yield of CAT production, calcualted by ssFBA for three different cases: constrained by transcription/translation (TX/TL) rates (black), same as previous but without amino acid synthesis reactions (medium gray), and same as previous but constrained by experimental measurements where available (light gray). Error bars represent standard deviation of the ensemble.
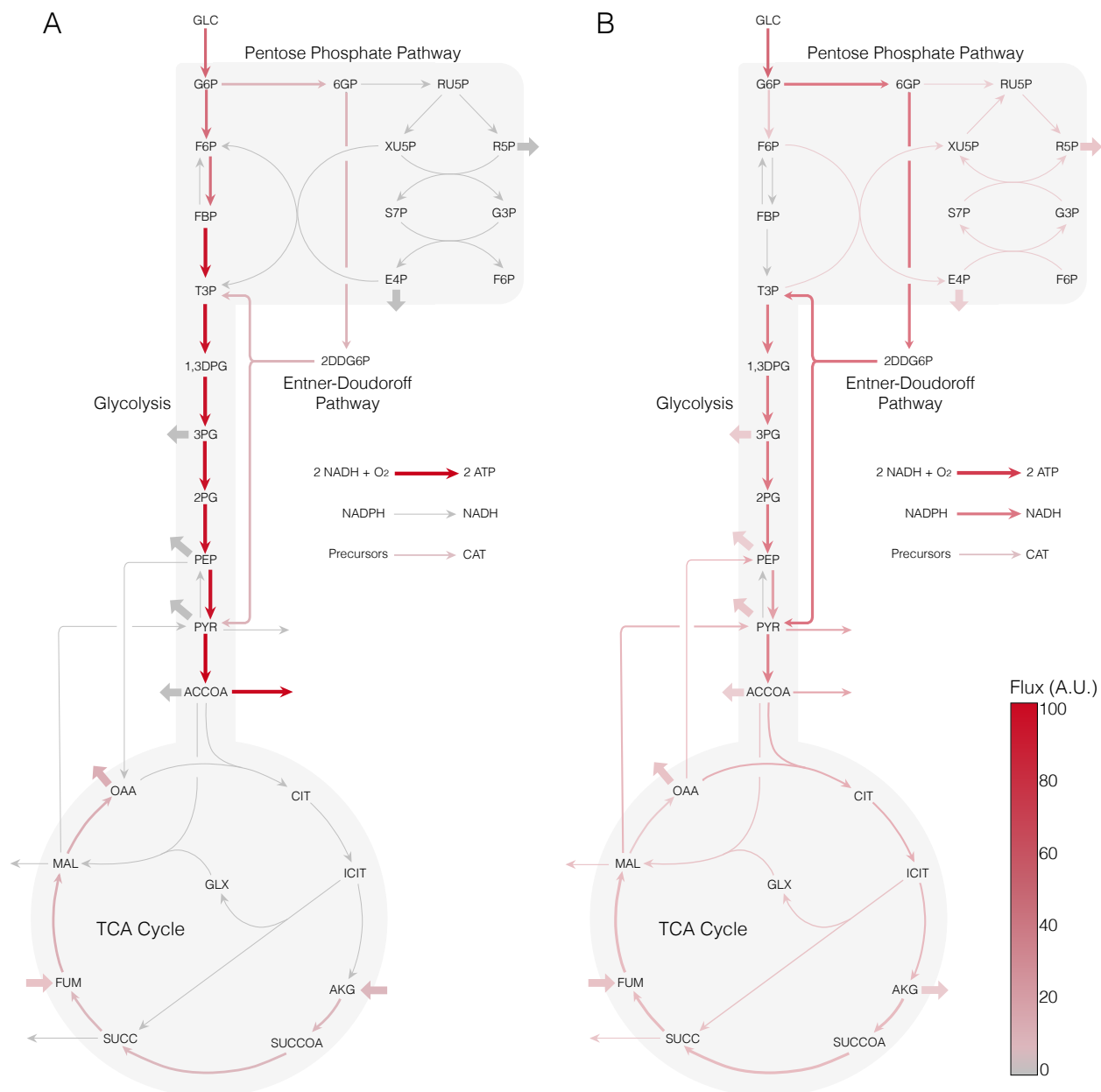
**Fig. 9:** Flux profile for glycolysis, pentose phosphate pathway, Entner-Doudoroff pathway, TCA cycle, NADPH/NADH transfer, oxidative phosphorylation, and protein synthesis. Thicker and redder arrows signify larger flux values (see colorbar). A. ssFBA constrained by transcription and translation rates, with or without amino acid synthesis reactions. B. ssFBA constrained by transcription and translation rates and experimental measurements where available.

**Table 1:** CAT carbon yield breakdown for best-fit set, knockouts, and experimental data. Carbon produced as CAT, carbon consumed as glucose and each amino acid, sum of consumed species, and yield. Accumulation of alanine and glutamine (negative consumption terms) was not considered in yield calculation.

| Carbon Produced (C-mM) | Best-fit | $\triangle$app | $\triangle$nuo | $\triangle$cyd | $\triangle$app $\triangle$nuo $\triangle$cyd | Data |
|---|---|---|---|---|---|---|
| CAT | 20.9 | 21.4 | 18.1 | 6.5 | 5.1 | 21.6 |
| Carbon Consumed (C-mM) | | | | | | |
| GLC | 215.4 | 215.4 | 215.4 | 215.4 | 159.8 | 215.4 |
| ALA | -11.6 | -11.4 | 1.7 | -3.8 | -3.2 | -12.1 |
| ASN | 6.2 | 6.2 | 6.2 | 6.3 | 6.3 | 6.3 |
| ASP | 7.5 | 7.5 | 3.9 | 0.0 | 0.0 | 9.6 |
| CYS | 3.0 | 3.1 | 3.0 | 2.9 | 2.9 | 3.7 |
| GLN | -11.4 | -11.3 | -4.0 | 1.8 | 2.7 | -11.7 |
| GLY | 3.1 | 3.1 | 2.6 | 1.1 | 0.9 | 1.5 |
| HIS | 0.2 | 0.2 | 1.1 | 0.4 | 0.3 | 0.0 |
| ILE | 1.0 | 1.0 | 0.8 | 0.3 | 0.2 | 1.7 |
| LEU | 1.4 | 1.4 | 1.2 | 0.4 | 0.3 | 2.0 |
| LYS | 10.7 | 10.7 | 13.1 | 13.2 | 13.2 | 8.3 |
| MET | 0.8 | 0.8 | 0.7 | 0.2 | 0.2 | 2.9 |
| PHE | 3.2 | 3.3 | 2.8 | 1.0 | 0.8 | 1.6 |
| PRO | 2.4 | 2.4 | 0.7 | 0.2 | 0.2 | 1.9 |
| SER | 2.5 | 2.5 | 2.4 | 2.1 | 2.1 | 1.8 |
| THR | 3.4 | 3.4 | 3.3 | 2.9 | 2.8 | 2.8 |
| TRP | 1.0 | 1.0 | 0.8 | 0.3 | 0.2 | 1.2 |
| TYR | 1.1 | 1.1 | 1.1 | 0.4 | 0.4 | 0.6 |
| VAL | 1.4 | 1.5 | 1.2 | 0.4 | 0.4 | 2.4 |
| Sum | 264.3 | 264.6 | 262.0 | 249.3 | 193.7 | 263.7 |
| Yield | 7.9% | 8.1% | 6.9% | 2.6% | 2.7% | 8.2% |
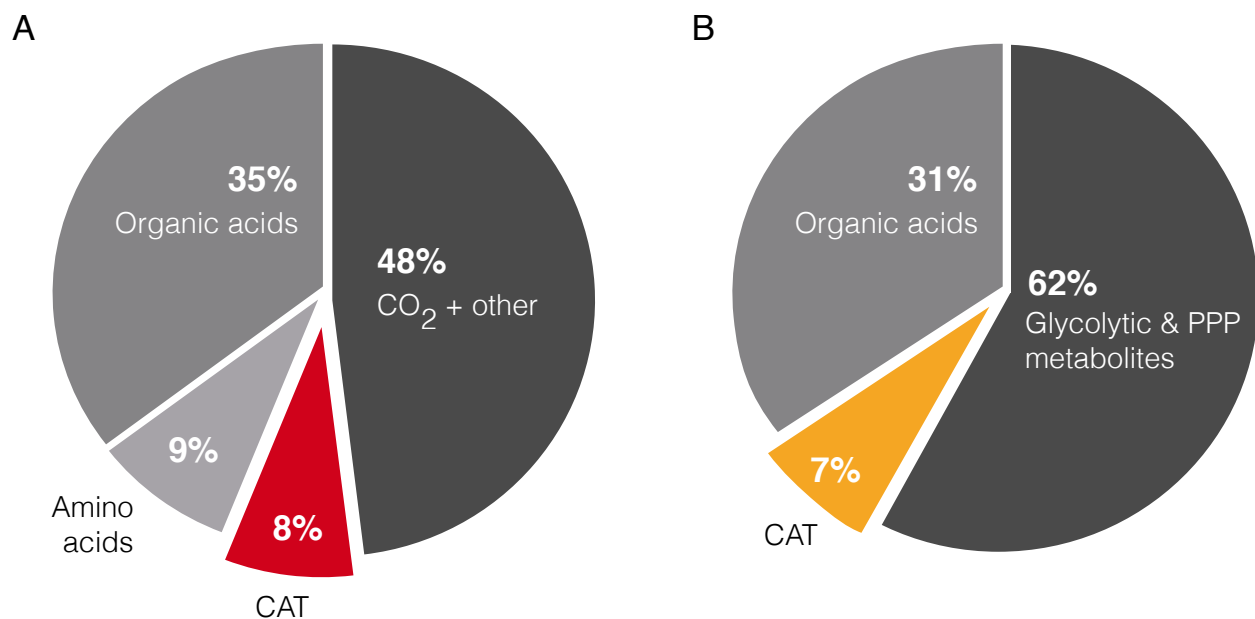
**Fig. 10:** Carbon and energy balances for the best-fit set. A. Carbon moles produced as CAT, amino acids (alanine and glutamine), organic acids (lactate, acetate, succinate, and malate), and other byproducts including carbon dioxide, as percentages of total carbon consumption (glucose and all other amino acids). B. Energy cost of CAT production, accumulation of organic acids (lactate, acetate, succinate, and malate), and glycolytic and pentose phosphate metabolites, as percentages of total energy utilization from glucose. Energy costs calculated in terms of equivalent ATP molecules.
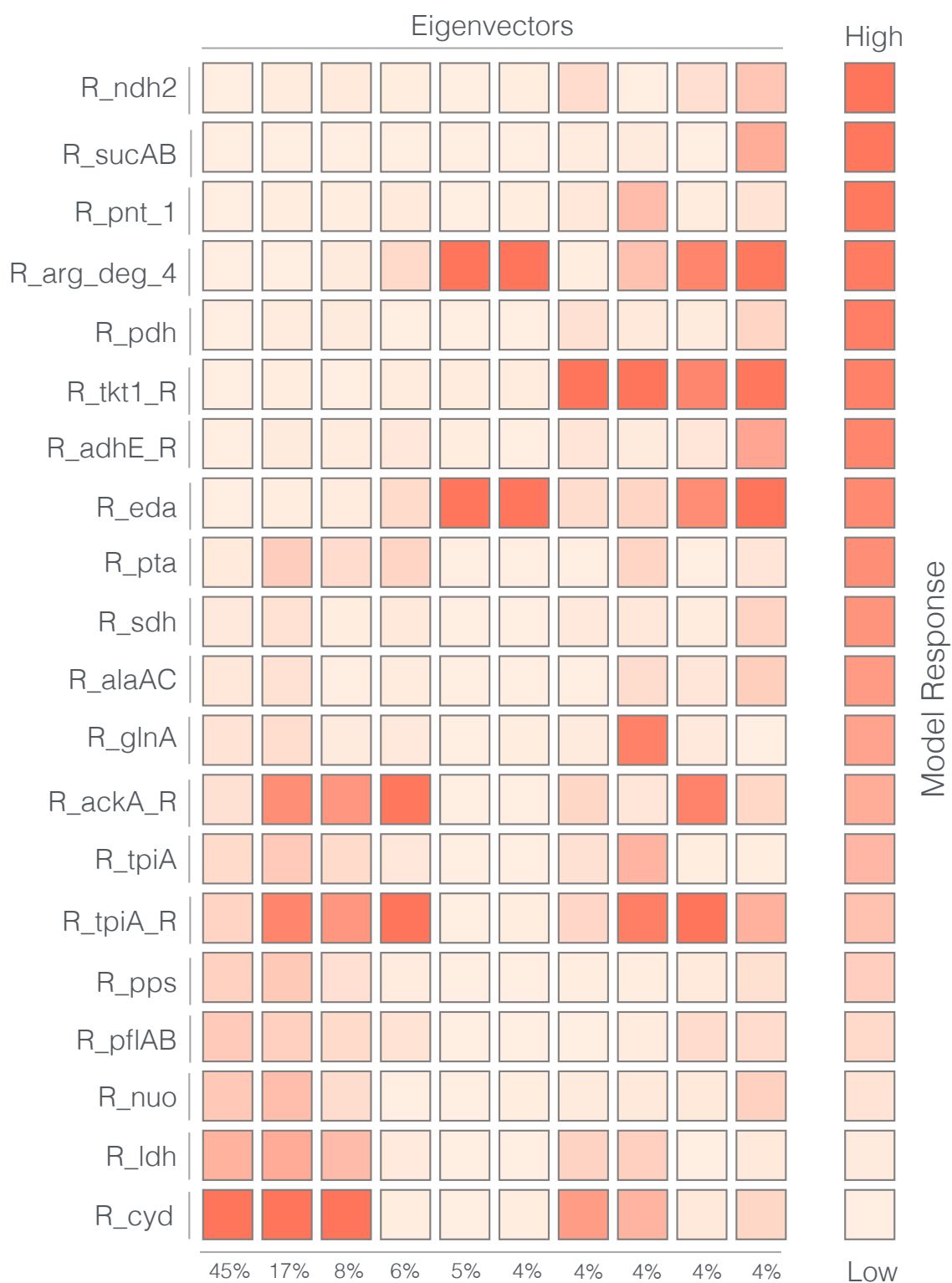
**Fig. S1:** Sensitivity of system state to model parameters, decomposed into eigenmodes. Sensitivity of top 10 eigenvectors (columns, left to right) to top 20 most influential parameters (rows, bottom to top). Relative magnitudes of eigenvalues expressed as percentages.